

Supporting Information for “Regional inversion shows promise in capturing extreme-event-driven CO₂ flux anomalies but is limited by atmospheric CO₂ observational coverage”

B. Byrne¹, J. Liu^{1,2}, K. W. Bowman^{1,3}, Y. Yin^{2,*}, J. Yun¹, G. D. Ferreira⁴,

S. M. Ogle^{4,5}, L. Baskaran¹, L. He⁶, X. Li⁷, J. Xiao⁸, K. J. Davis⁹

¹Jet Propulsion Laboratory, California Institute of Technology, Pasadena, CA, USA

²Division of Geological and Planetary Sciences, California Institute of Technology, Pasadena, CA, USA

³Joint Institute for Regional Earth System Science and Engineering, University of California, Los Angeles, USA

⁴Natural Resource Ecology Laboratory, Colorado State University, Fort Collins, CO 80523, United States of America

⁵Department of Ecosystem Science and Sustainability, Colorado State University, Fort Collins, CO 80523, United States of America

⁶Department of Global Ecology, Carnegie Institution for Science, Stanford, CA, United States of America

⁷Research Institute of Agriculture and Life Sciences, Seoul National University, Seoul, South Korea

⁸Earth Systems Research Center, Institute for the Study of Earth, Oceans, and Space, University of New Hampshire, Durham, NH,

USA

⁹Department of Meteorology and Atmospheric Science, and Earth and Environmental Systems Institute, The Pennsylvania State

University, University Park, Pennsylvania

*Now at Department of Environmental Studies, New York University, New York, NY, USA

©2023. All rights reserved. California Institute of Technology, government sponsorship acknowledged.

Contents of this file

1. Text S1 to S2
2. Figures S1 to S15

Text S1.

This section provides an extended description of the comparison of posterior CO₂ fields with independent aircraft CO₂ measurements. Co-samples were made for all aircraft measurements that were deemed assimilable in version 8.0 of the the NOAA GLOBALVIEW plus Obspack dataset (Schuldt et al., 2022). To simplify the analysis, we examine three regions over North America, shown in Fig. S7. We aggregate temporally to weekly mean obs minus model mismatches within each region, to better match the timescale being optimized in the inversions. Figure S8 shows plots of the obs minus model statistics across all weeks in each region for the boundary layer (<2000 m) and free troposphere (>2000 m), while Figs. S9–S11 show vertical profiles of the obs minus model differences for each week. Overall, we find that both the prior and posterior CO₂ fields show close agreement to independent aircraft CO₂ observations, with differences close to expected representativeness errors. The obs-model mismatches do not show large differences between flux estimates, suggesting that the data-model mismatch has limited sensitivity to flux estimates on the scale optimized (weekly, 4° × 5°), and may be largely driven by transport errors and higher spatial and temporal flux variations. Nevertheless, the posterior CO₂ fields generally show smaller mean biases. Overall, the LNLGOGIS experiment shows the smallest biases, suggesting that additional data improves regional flux estimates (despite concerns about the quality of ocean glint data (Byrne et al., 2023)). That said, the obs minus model differences are quite small for all cases.

Finally, we examine the obs minus model differences for ΔNEE -sensitive observations. To find ΔNEE -sensitive observations, we simulate an atmospheric CO_2 pulse using bottom-up ΔNEE for 2018 and 2019, then define any observation with a signal greater than 0.5 ppm to be ΔNEE -sensitive. Figure S12 shows the obs minus model differences for ΔNEE -sensitive observations during 2018 and 2019. All experiments are found to show close agreement with the observations. Overall, we find that the LNLGOGIS shows a slightly smaller bias than the other experiments.

Text S2.

This section provides an extended description of a set of flux inversions with imposed prior IAV. For these experiments, prior IAV is introduced by imposing year-specific bottom-up NPP estimates (assumed to equal $0.65 \times \text{GPP}$) in the prior, and optimizing climatological HR. Note that the experiments with a climatological prior impose 2018-2019 mean NPP for both years.

Figures S13–S15 show the posterior ΔNEE estimates for the prior with imposed IAV. The spatial structures in IAV correspond closely to both the prior and inversions using climatological priors. However, the magnitude of ΔNEE is generally much increased for both the US Midwest (Fig. S13) and other regions within CONUS (Fig. S15). The increase in magnitude is consistent with OSSEs, suggesting that the climatological priors underestimate the magnitude of the anomalies, however the relative accuracy of these inversions is difficult to quantify.

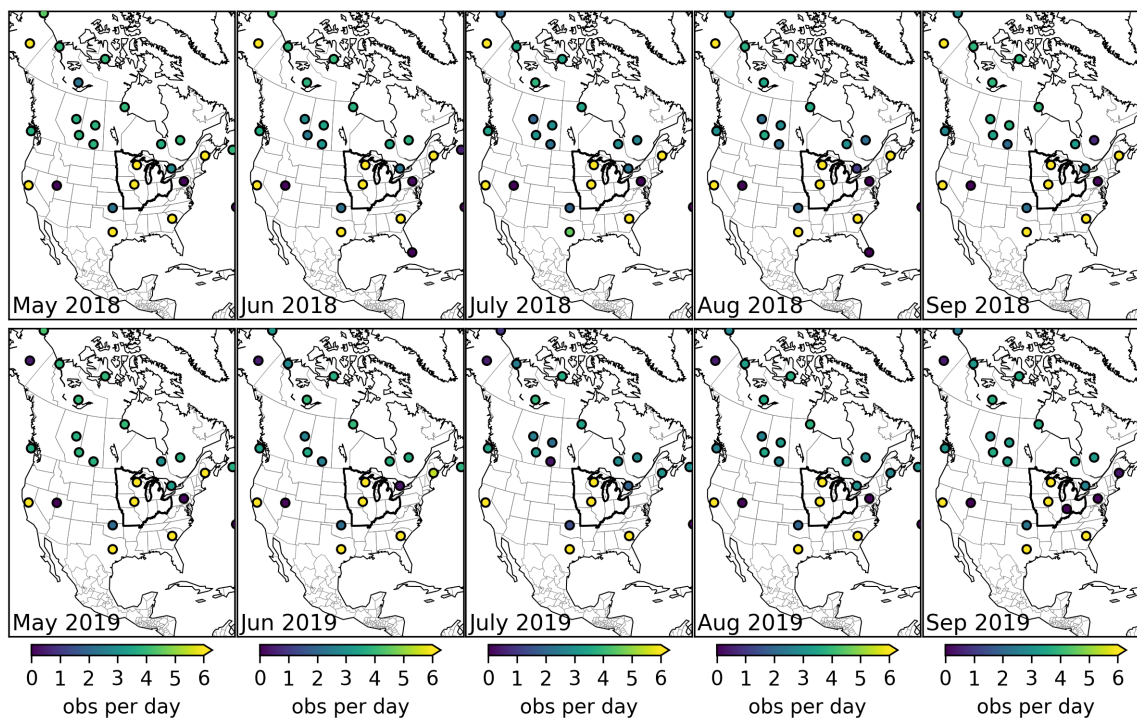


Figure S1. Monthly observational coverage of assimilated in situ measurements over North America for May–Sep during 2018 and 2019. Note that measurements over Canada end in July of 2019.

References

- Byrne, B., Baker, D. F., Basu, S., Bertolacci, M., Bowman, K. W., Carroll, D., ... Zeng, N. (2023). National CO₂ budgets (2015–2020) inferred from atmospheric CO₂ observations in support of the global stocktake. *Earth System Science Data*, 15(2), 963–1004. Retrieved from <https://essd.copernicus.org/articles/15/963/2023/> doi: 10.5194/essd-15-963-2023
- Schuldt, K. N., Mund, J., Luijckx, I. T., Aalto, T., Abshire, J. B., Aikin, K., ... van den Bulk, P. (2022). *Multi-laboratory compilation of atmospheric carbon dioxide data for the period 1957–2021; obspack_co2_1_globalviewplus_v8.0_2022-08-27*. NOAA Global Monitoring Laboratory. doi: 10.25925/20220808

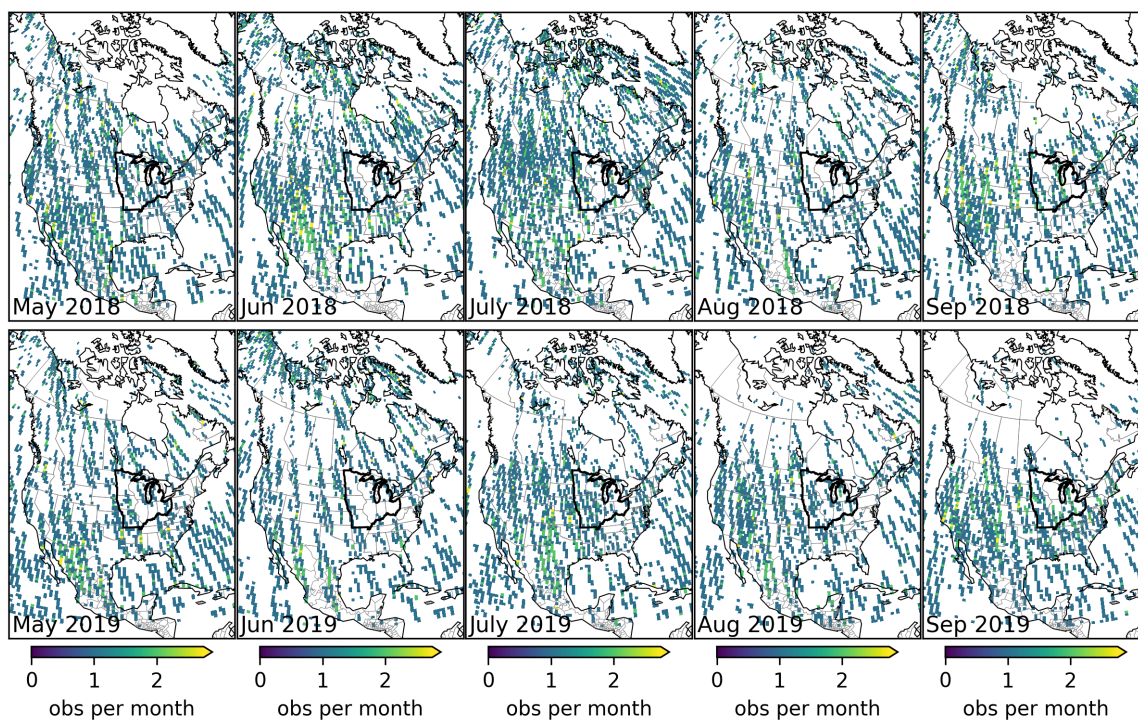


Figure S2. Monthly observational coverage of assimilated OCO-2 X_{CO_2} retrievals over North America for May–Sep during 2018 and 2019.

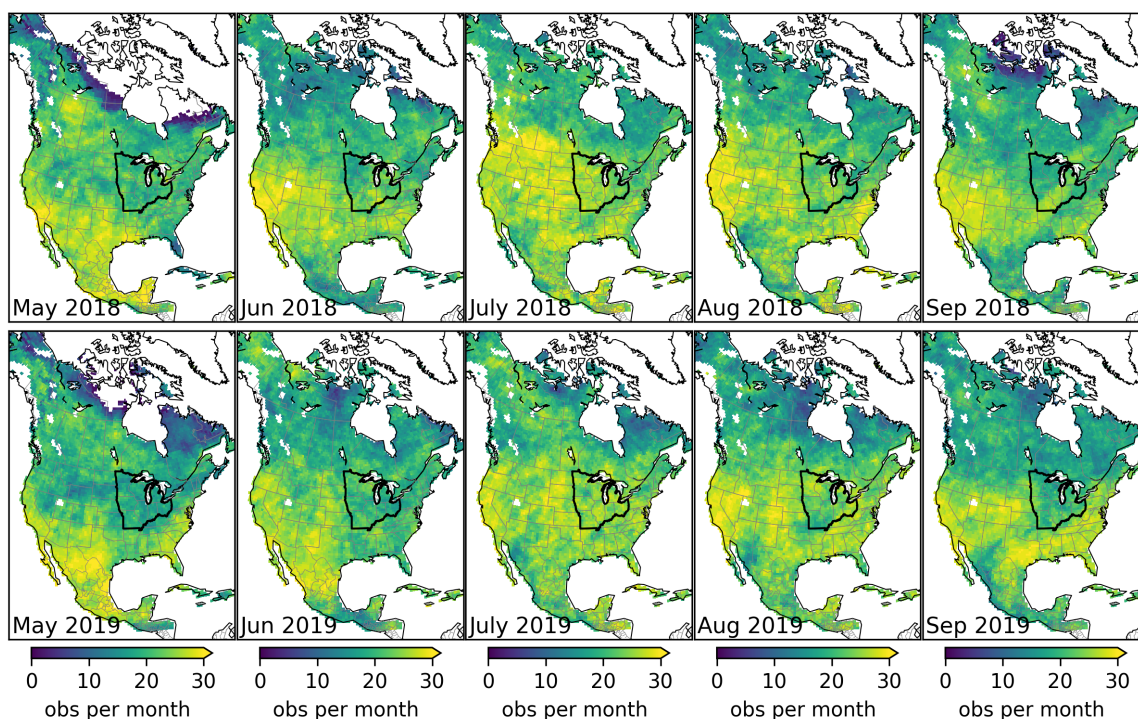


Figure S3. Monthly observational coverage of assimilated ideal LEO pseudo- X_{CO_2} retrievals over North America for May–Sep during 2018 and 2019.

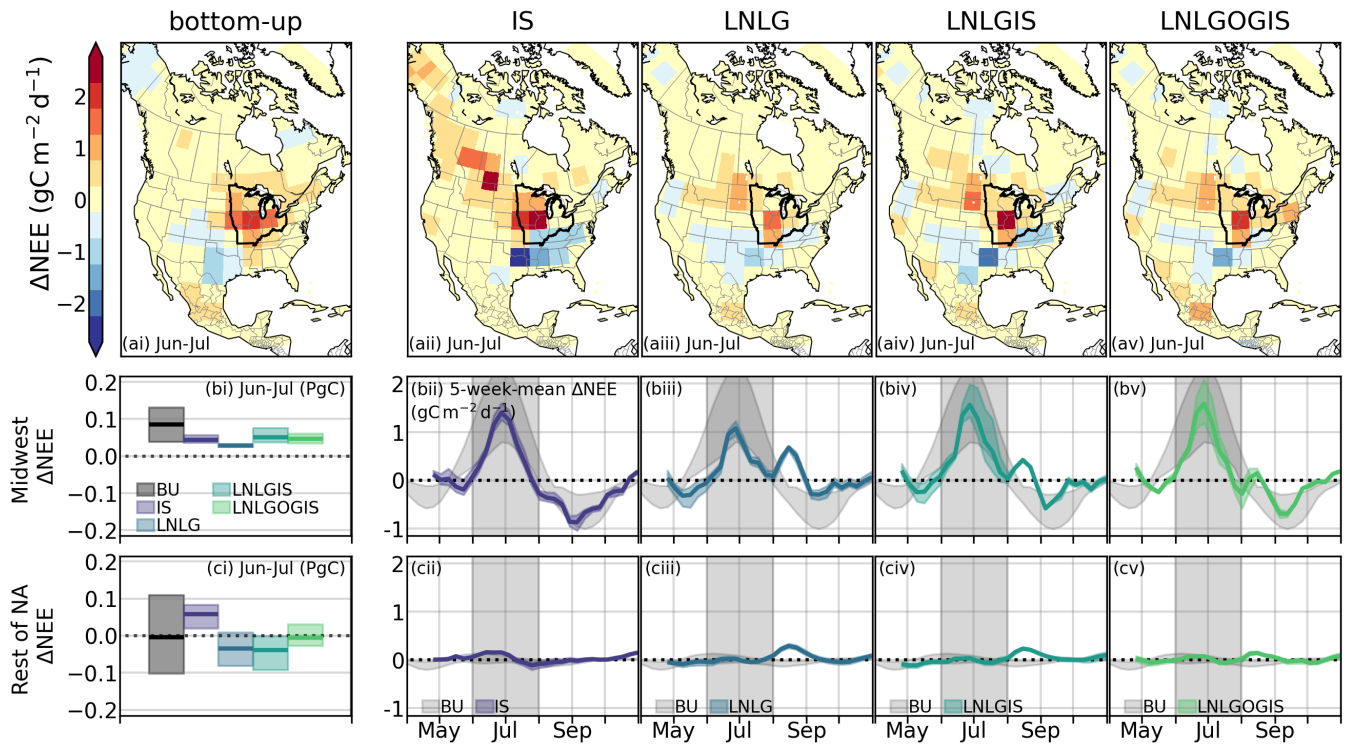


Figure S4. ΔNEE for each one-way nested atmospheric CO_2 inversion experiment. Top row show June-July maps of the mean ΔNEE for each experiment. Second row shows the ΔNEE within the MidWest and across the rest of North America. Bottom row shows the weekly ΔNEE within the MidWest after applying a 5-week running mean.

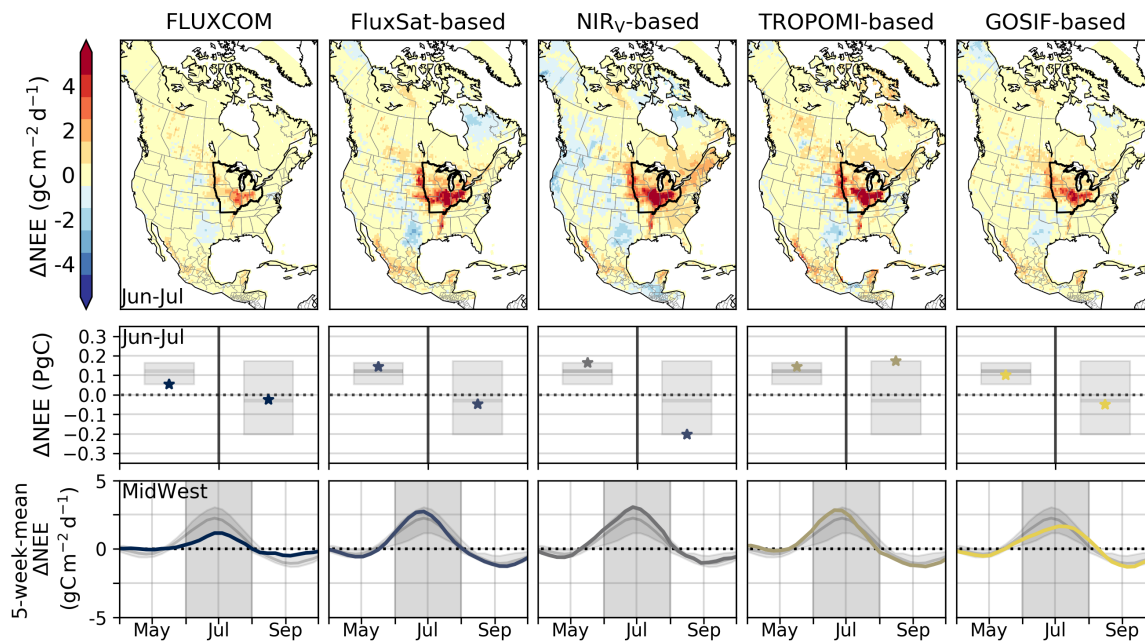


Figure S5. Δ NEE for each bottom-up estimate (best estimate, CUE=0.6). Top row show June–July maps of the mean Δ NEE for each estimate. Second row shows the Δ NEE within the Midwest (on left) and across the rest of North America (on right). Bottom row shows the weekly Δ NEE within the Midwest after applying a 5-week running mean.

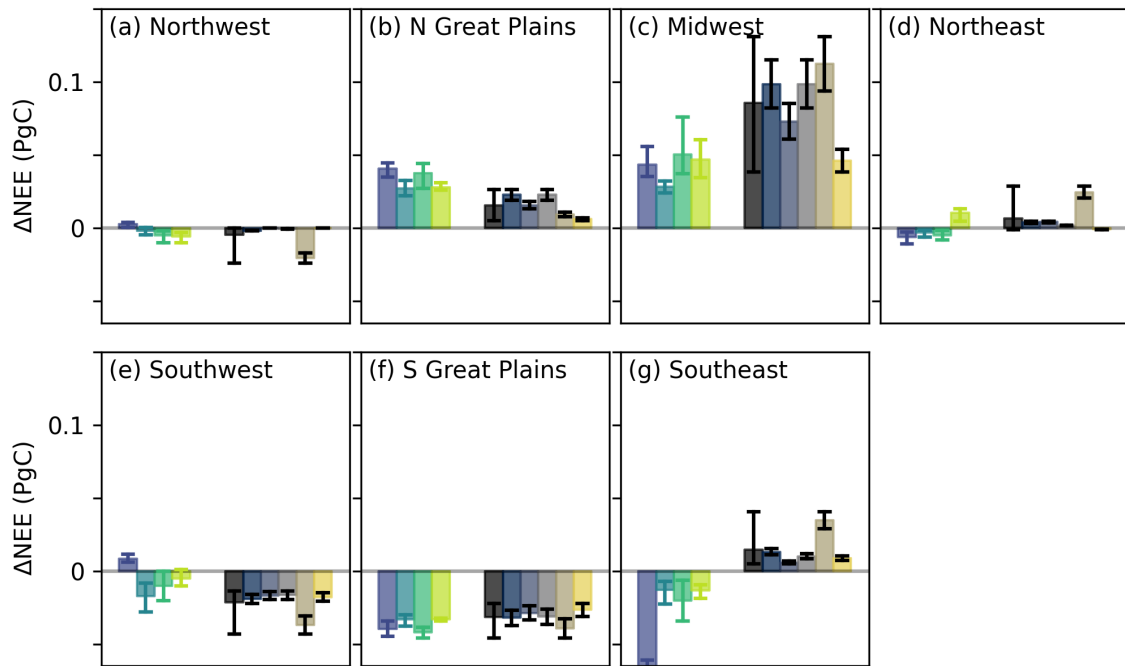


Figure S6. June–July Δ NEE over CONUS National Climate Assessment Regions (https://scenarios.globalchange.gov/regions_nca4).

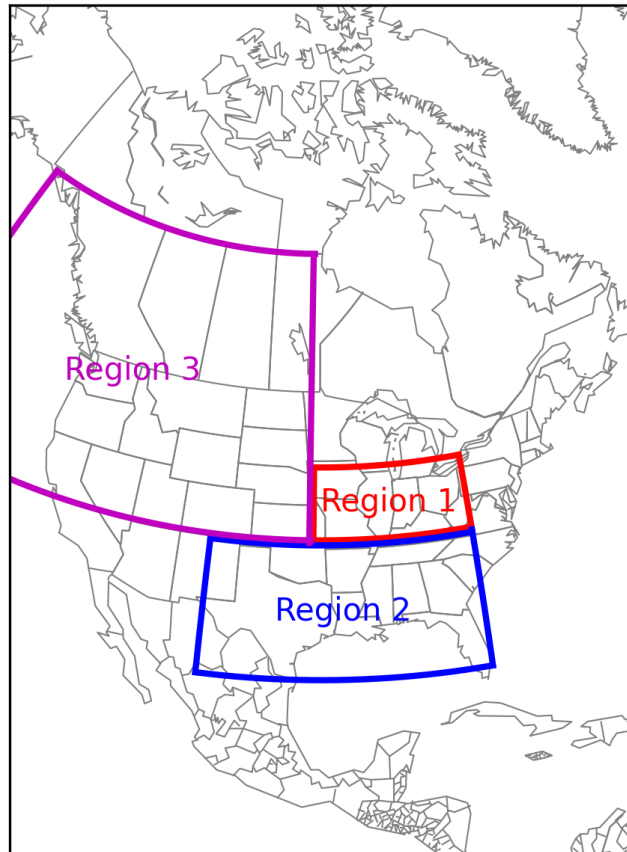


Figure S7. Regions defined for aircraft observation comparisons.

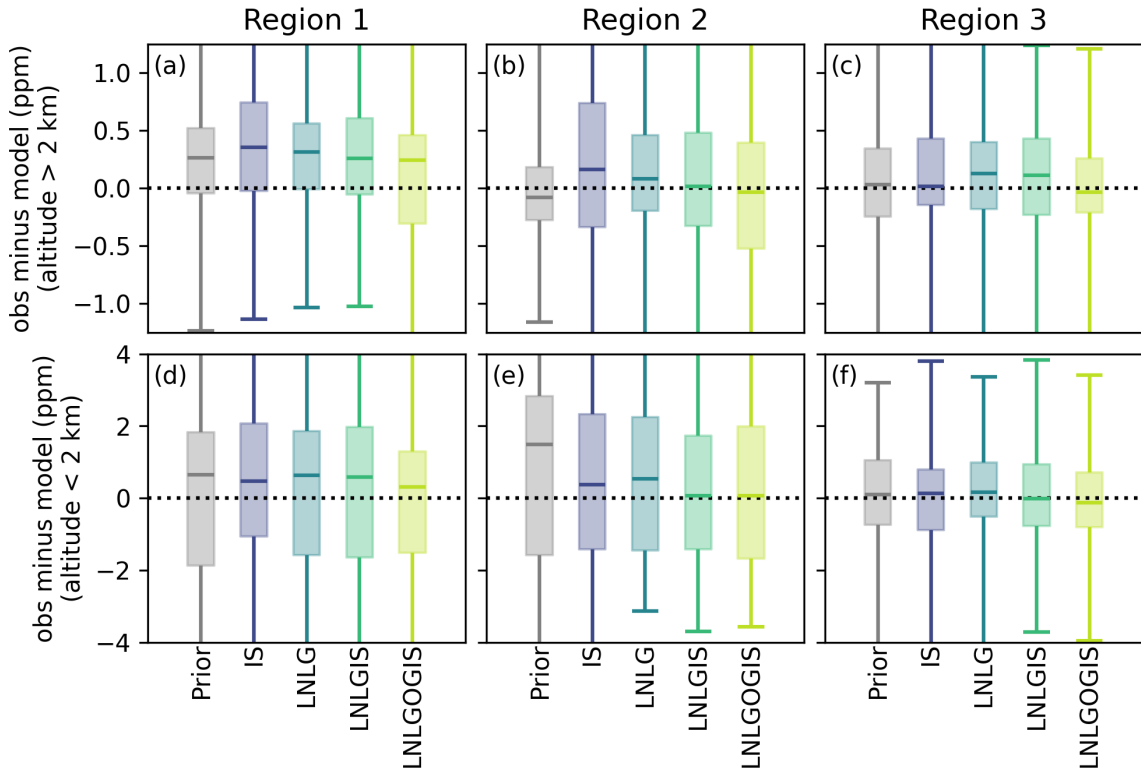


Figure S8. Statistics of weekly obs minus model differences for each region. Differences are shown for both (a-c) the free troposphere and (d-f) the boundary layer. The horizontal line shows the median difference, boxed area shows 25th–75th percentile range and lines show the 0th–100th percentile range.

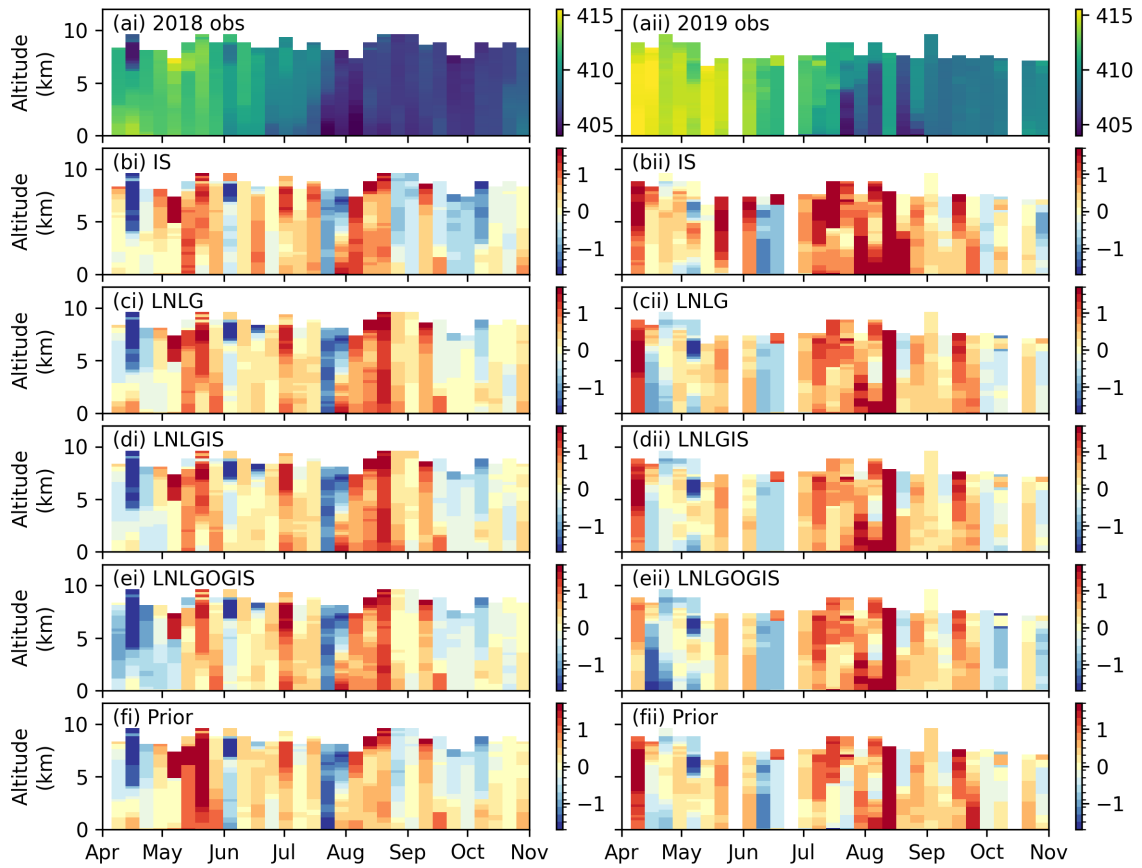


Figure S9. Weekly mean vertical profiles of CO_2 (250 m vertical grid) for all aircraft measurements over Region 1. Aircraft measurements are shown on row (a), with the obs minus model differences shown on the lower rows. Weeks for 2018 and 2019 are shown in columns (i) and (ii), respectively.

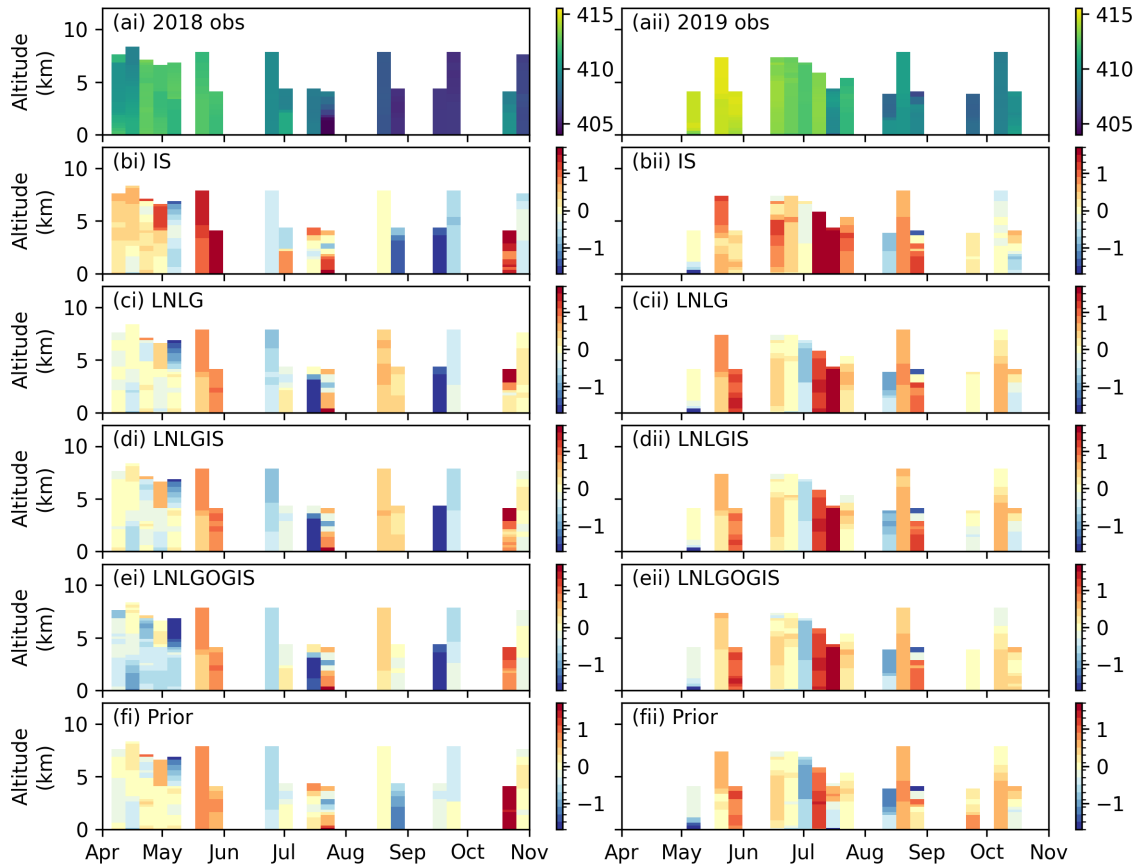


Figure S10. Weekly mean vertical profiles of CO₂ (250 m vertical grid) for all aircraft measurements over Region 2. Aircraft measurements are shown on row (a), with the obs minus model differences shown on the lower rows. Weeks for 2018 and 2019 are shown in columns (i) and (ii), respectively.

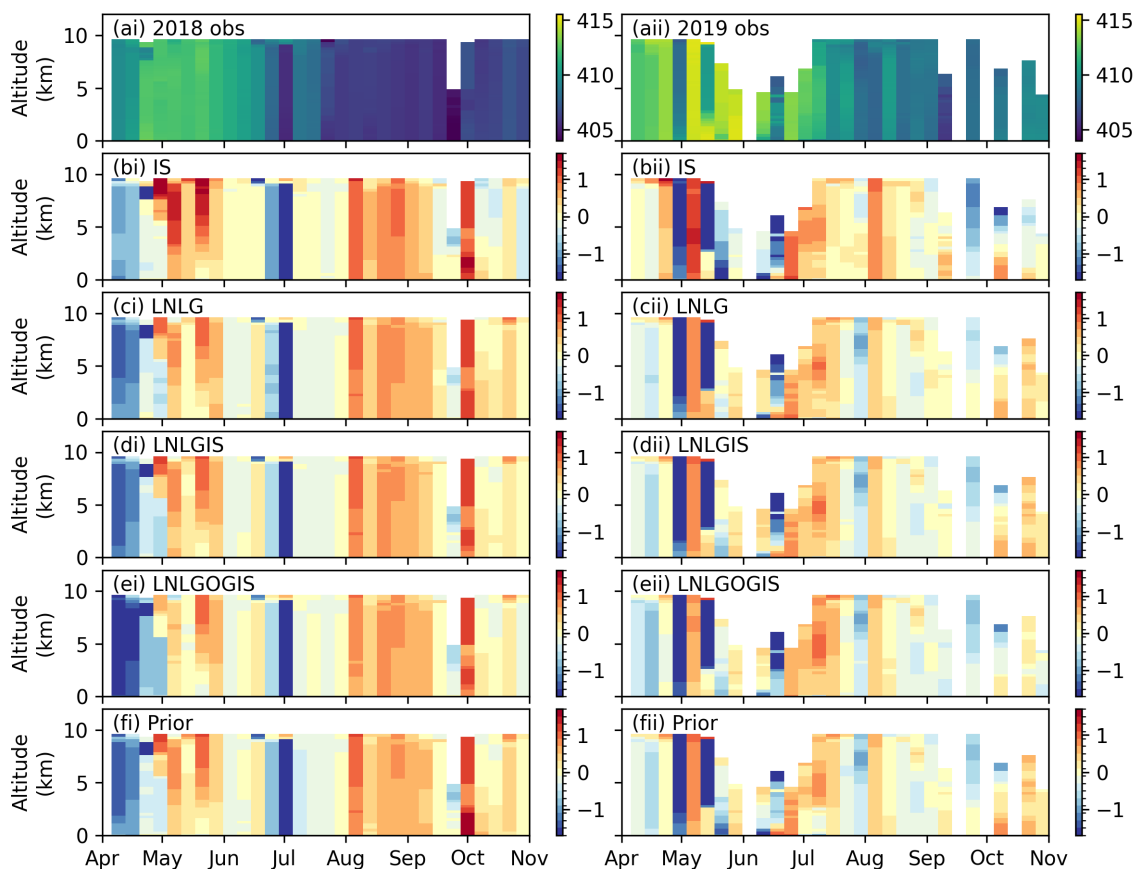


Figure S11. Weekly mean vertical profiles of CO₂ (250 m vertical grid) for all aircraft measurements over Region 3. Aircraft measurements are shown on row (a), with the obs minus model differences shown on the lower rows. Weeks for 2018 and 2019 are shown in columns (i) and (ii), respectively.

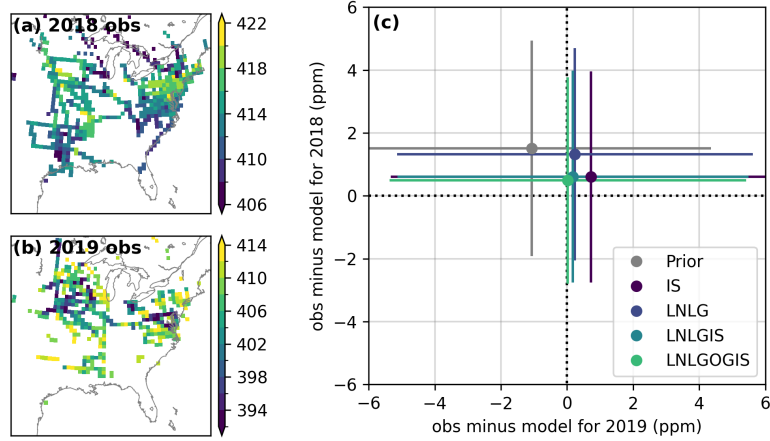


Figure S12. Median plus/minus standard deviation of the obs minus model difference for Δ NEE-sensitive atmospheric CO₂ measurements in 2018 versus 2019 (see Text S1). These statistics are calculated across all individual observations that qualify as flood-sensitive.

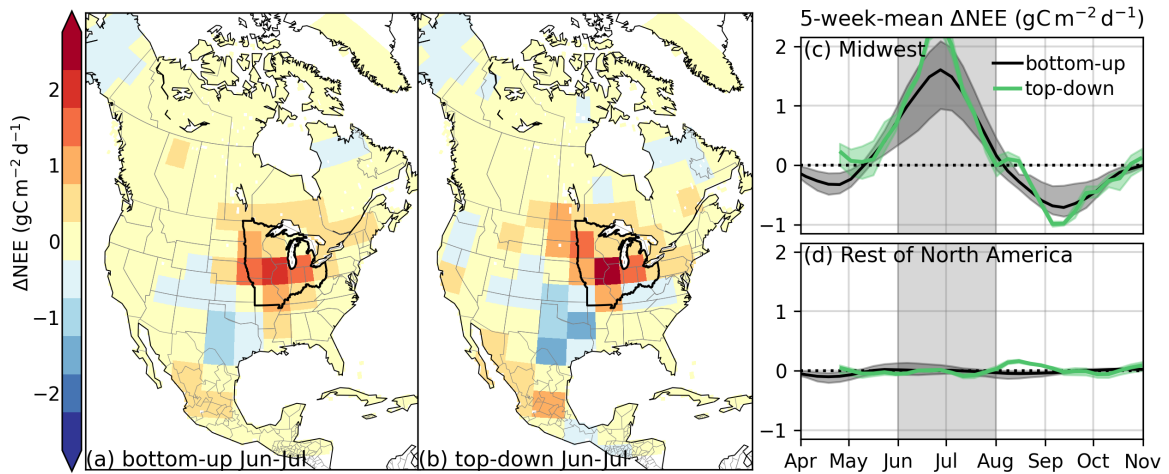


Figure S13. Same as Fig. 1 but for inversions with prior IAV prescribed. (a) Bottom-up and (b) top-down (LNLGOGIS) spatial patterns of June–July mean Δ NEE at $4^\circ \times 5^\circ$ spatial resolution. (c) US Midwest and (d) rest of North America 5-week-mean Δ NEE. The US Midwest is defined as the area within Illinois, Indiana, Iowa, Michigan, Minnesota, Missouri, Ohio, and Wisconsin and is indicated by the black outline in panels (a) and (b).

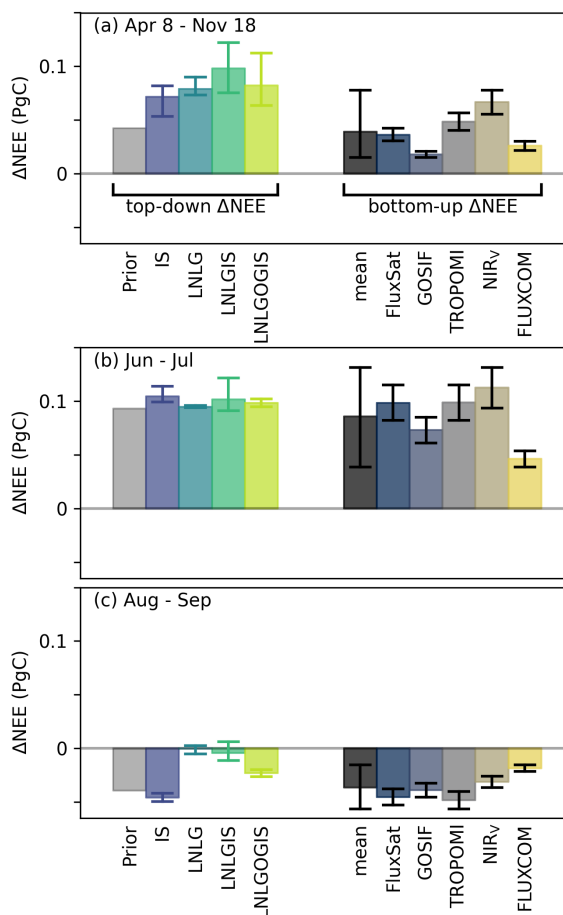


Figure S14. Same as Fig. 2 but for inversions with prior IAV prescribed. Top-down ΔNEE , bottom-up ΔNEE , and yield-based ΔNPP for crops ($\Delta\text{NPP}_{\text{crop}}$) over the US Midwest. ΔNEE is calculated for (a) the entire inversion period (April 8th – Nov 18th), (b) June-July and (c) Aug-Sep. The top-down estimates show the mean and range obtained using three different priors.

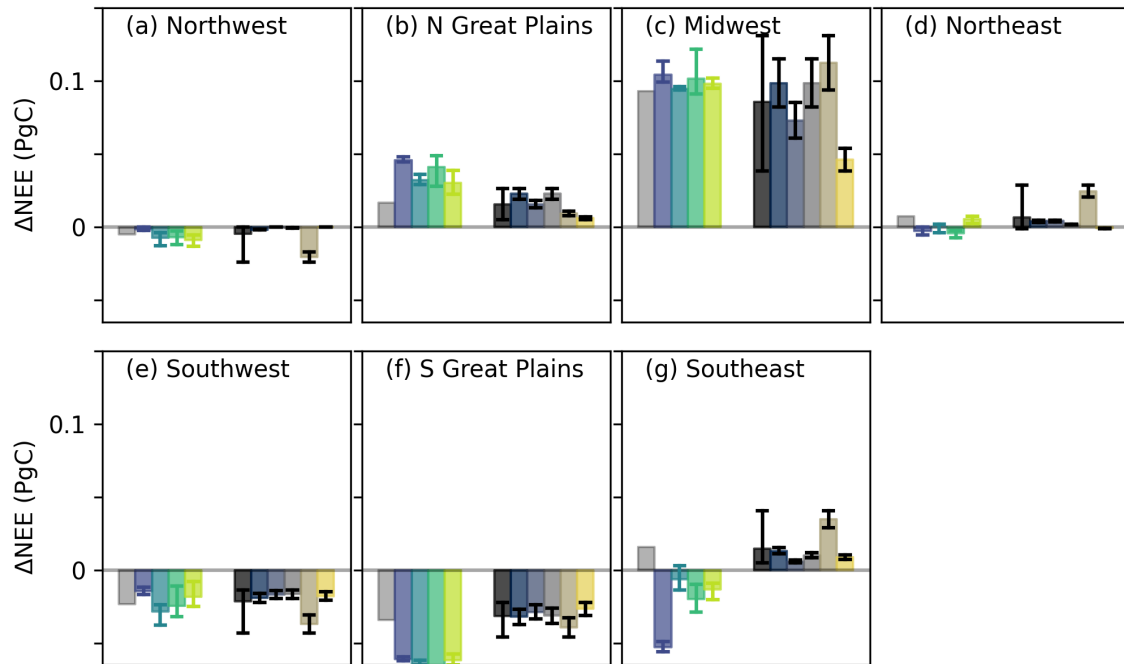


Figure S15. Same as Fig. S6 but for inversions with prior IAV prescribed. June–July ΔNEE over CONUS National Climate Assessment Regions (https://scenarios.globalchange.gov/regions_nca4) for top-down estimates with prior IAV.